

# The GLUEX Start Counter Detector

E. Pooser<sup>a,b</sup>, F. Barbosa<sup>a</sup>, W. Boeglin<sup>b,\*</sup>, C. Hutton<sup>a</sup>, M. Ito<sup>a</sup>, M. Kamel<sup>b</sup>, P. Khetarpal<sup>b</sup>, A. LLodra<sup>b</sup>, N. Sandoval<sup>a</sup>, S. Taylor<sup>a</sup>, C. Yero<sup>b</sup>, T. Whitlatch<sup>a</sup>, S. Worthington<sup>a</sup>, B. Zihlmann<sup>a</sup>

<sup>a</sup>*Thomas Jefferson National Accelerator Facility, Newport News, VA 23606, USA*

<sup>b</sup>*Florida International University, Miami, FL, 33199, USA*

---

## Abstract

The design, fabrication, calibration, and performance of the GLUEX Start Counter detector is described. The Start Counter detector was designed to operate at photon intensities of up to  $10^8 \gamma/s$  in the coherent peak and provides a timing resolution of  $\approx 250$  ps thus providing successful identification of the photon beam buckets to more than 99% accuracy. Furthermore, the Start Counter detector provides excellent solid angle coverage,  $\sim 90\%$  of  $4\pi$  hermeticity, a high degree of segmentation for background rejection, and is utilized in the level 1 trigger for the experiment. It consists of a cylindrical array of 30 thin scintillators with pointed ends that bend towards the beam at the downstream end. Magnetic field insensitive silicon photomultiplier detectors were selected as the readout system.

**Keywords:** Attenuation, F1 TDC, Flash 250 MHz ADC, GLUEX, Multi-Pixel Photon Counter, Particle Identification, Plastic Scintillator, Polishing Scintillators, Propagation Time, Silicon Photomultiplier, Time of Flight, Time-walk, Trigger

---

## 1. Introduction

The GLUEX experiment, staged in Hall D at the Thomas Jefferson National Accelerator Facility (TJNAF), primarily aims to study the rich spectrum of photo-produced mesons with unprecedented statistics. The coherent bremsstrahlung technique is implemented to produce a linearly polarized photon beam incident on a liquid H<sub>2</sub> target. A Start Counter detector was fabricated to properly identify the photon beam buckets and to provide accurate timing information.

## 2. Design

In this section we discuss the details of the GLUEX Start Counter design. The general engineering specifics pertaining to the scintillators, support structure, detector readout system and electronics are discussed.

### 2.1. Overview

The Start Counter (ST) detector, seen in Fig. 1, surrounds a 30 cm long super cooled liquid H<sub>2</sub> target while providing  $\sim 90\%$  of  $4\pi$  solid angle coverage relative to the target center. The primary

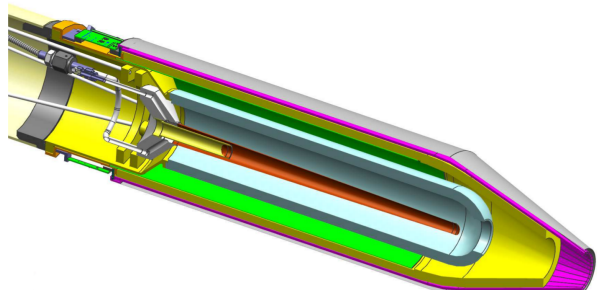


Figure 1: The GLUEX Start Counter mounted to the LH<sub>2</sub> target.

purpose of the ST detector is, in coincidence with the tagger, to properly identify the photon beam bucket associated with detected particles produced via linearly polarized photons incident on the target. It is designed to operate at tagged photon intensities of up to  $10^8 \gamma/s$  in the coherent peak.

---

\*Corresponding Author

Email address: boeglinw@fiu.edu (W. Boeglin)

Moreover, the ST has a high degree of segmentation for background rejection, is utilized in particle identification, and is a primary component of the level 1 trigger of the GLUEX experiment during high luminosity running[1].

The ST detector consists of an array of 30 scintillators with pointed ends that bend towards the beam at the downstream end. EJ-200 scintillator

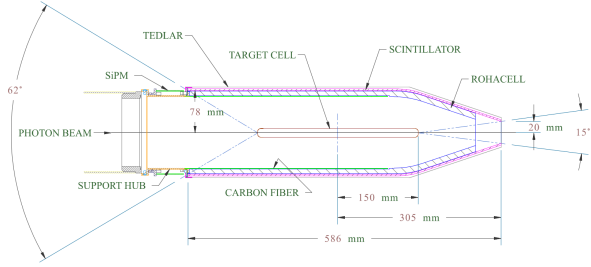


Figure 2: Labeled 2-D cross section of the Start Counter detector.

material from Eljen Technology[2], which has a decay time of 2.1 ns and a long attenuation length[3], was selected for this application. The amount of support structure material was kept to an absolute minimum in the active region of the detector and is made up of low density Rohacell[4]. Silicon Photomultiplier (SiPM) detectors were selected as the readout system. The detectors are not affected by the high magnetic field produced by the superconducting solenoid magnet. Moreover, the SiPMs were placed as close as possible to the upstream end of each scintillator element, thereby minimizing the loss of scintillation light[1].

## 2.2. Scintillator Paddles

Each individual paddle of the Start Counter was machined from a long, thin, polyvinyltoluene plastic EJ-200 scintillator bar that was diamond milled to be 600 mm in length, 3 mm thick, and  $20 \pm 2$  mm wide, by Eljen Technology. Each scintillator was bent around a highly polished aluminum drum by applying localized infrared heating to the bend region. The bent scintillator bars were then sent to McNeal Enterprises Inc.[5], a plastic fabrication company, where they were machined to the desired geometry illustrated in Fig. 3.

The paddles consist of three sections and are described from the upstream to the downstream end of the target. The straight section is 39.5 cm in length while being oriented parallel to both the target cell and beamline.. The bend region is a

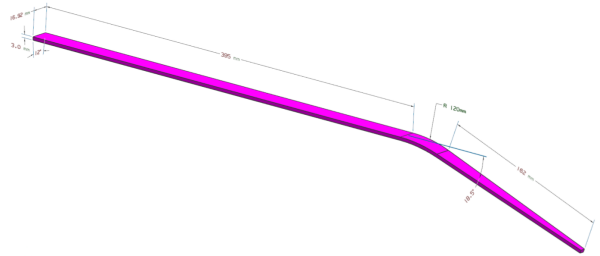


Figure 3: Start Counter single paddle geometry

18.5° arc of radius 120 cm and is downstream of the straight section. The tapered nose region is downstream of the target chamber and bends towards the beam line such that the tip of the nose is at a height of 2 cm above the beam line.

After the straight scintillator bar was bent to the desired geometry, the two flat surfaces that are oriented orthogonal to the wide, top and bottom, surfaces were cut at a 6° angle. During this process, the width of the top and bottom surfaces were machined to be 16.92 mm and 16.29 mm wide respectively. Thus, each of the paddles may be rotated 12° with respect to the paddle that preceded it so that they form a cylindrical shape with a conical end. This geometrical design for the ST increases solid angle coverage while minimizing multiple scattering.

## 2.3. Support Structure

The ST scintillator paddles are placed atop a low density Rohacell ( $\rho = 0.075 \text{ g/cm}^3$ ) foam support structure which envelopes the target vacuum chamber seen in Fig. 4. The Rohacell, which is 11 mm

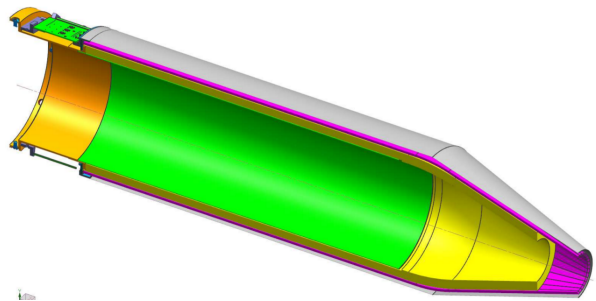


Figure 4: Cross section of the Start Counter support structure.

thick, is rigidly attached to the upstream support chassis and extends down the length of paddles however, not to include the last few centimeters of

the conical nose section. Glued to the inner diameter of the Rohacell support structure are 3 layers of carbon fiber ( $\rho = 1.523 \text{ g/cm}^3$ ) each of which are 95  $650 \mu\text{m}$  thick. A cross section of the ST can be seen in Fig. 4 where the carbon fiber is visible. The carbon fiber provides additional support during the assembly process as well as long term rigidity.

The various layers of material that comprise the ST support structure is illustrated in Fig. 5. In

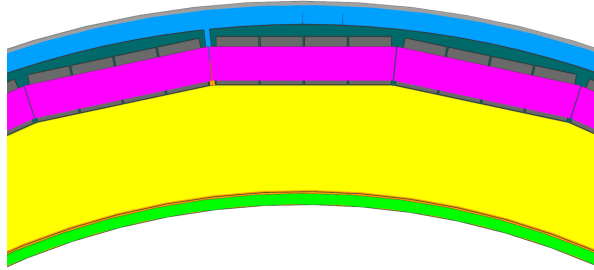


Figure 5: Start Counter materials.

order to ensure that the detector was light-tight, a plastic collar was placed around the top of the SiPMs at the upstream end as seen in Fig. 5. The collar served as a lip to which a cylindrical sheet 100 of black Tedlar was taped too. At the tip of the nose, a cone of Tedlar was then connected to the 105 aforementioned cylindrical section. To make the downstream end of the ST light-tight, another cone of Tedlar was taped to the nose of the inner Rohacell support structure and then attached to the top 110 Tedlar cone layer.

#### 2.4. SiPM Readout Detectors

The selected readout for each scintillator bar was 115 the magnetic field insensitive Hamamatsu S10931-050P surface mounted multi-pixel photon counters 120 (MPPCs)[6]. An individual  $3 \times 3 \text{ mm}^2$  MPPC, also known as a SiPM, in the aforementioned configuration is comprised of 3600 individual,  $50 \times 50 \mu\text{m}^2$ , Avalanche Photo-Diode (APD) pixel counters operating in Geiger mode. The signal output from 125 each SiPM is the total sum of the outputs from all 3600 APD pixels[7]. The scintillation light from an individual scintillator bar is collected by an array of four of these SiPMs.

The SiPM readout detectors are housed in a ceramic case which is surface mounted to a custom fabricated printed circuit board (PCB). The PCB is held in a fixed position while being attached to

the lip of the upstream chassis *via* two screws as illustrated in Fig. 6. The individual ST scintillators are coupled *via* an air gap ( $< 250 \mu\text{m}$ ) to groups of four SiPMs set in a circular arrangement as can be seen in Fig. 6.



Figure 6: ST1 of Start Counter read out system. The ST1's are rigidly attached to the upstream support chassis. Approximately 72% of the scintillator light is collected at the upstream end.

#### 2.5. Readout Electronics

The SiPMs reading out one individual paddle, are current summed prior to pre-amplification. The output of each preamp is then split; buffered for the analog to digital converter (ADC) output, and amplified for the time to digital converter (TDC) output by a factor five relative to the ADC. The ADC outputs are readout *via* JLab VME64x 250 MHz Flash ADC modules while the TDC outputs are input into JLab leading edge discriminators, followed by a high resolution 32 channel JLab VME64x F1TDC V2 module. Furthermore, each group of four SiPMs utilizes a thermocouple for temperature monitoring. There are 120 SiPMs in total, for a total of 30 pre-amplifier channels as seen Fig. 7.

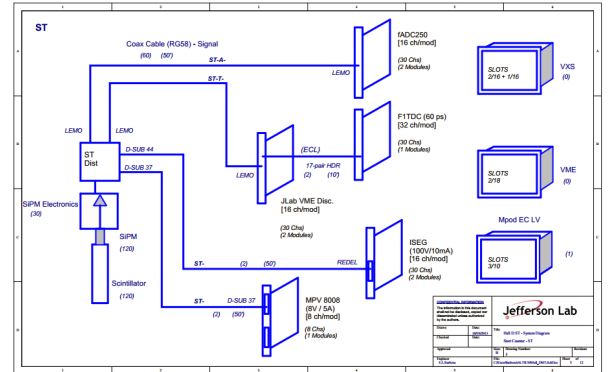


Figure 7: Start counter readout electronics diagram.

150 There are three components that comprise the ST detector readout system. The first component  
155 is the ST1 which holds 3 groups of 4 SiPMs as can be seen in Fig. 6. In order to mimic the geometry of the 30 paddle design one group of SiPM's is rotated by  $12^\circ$  relative to the central group, while the other adjacent group is rotated by  $-12^\circ$ . One ST1 unit will collect light from three paddles individually. The ST1 implements the current sum and bias distribution per group of 4 SiPMs. It also has a thermocouple for temperature monitoring.

160 The second component is the ST2, seen in Fig. 8, is a PCB that houses the signal processing electronics of the readout system. It has 3 channels

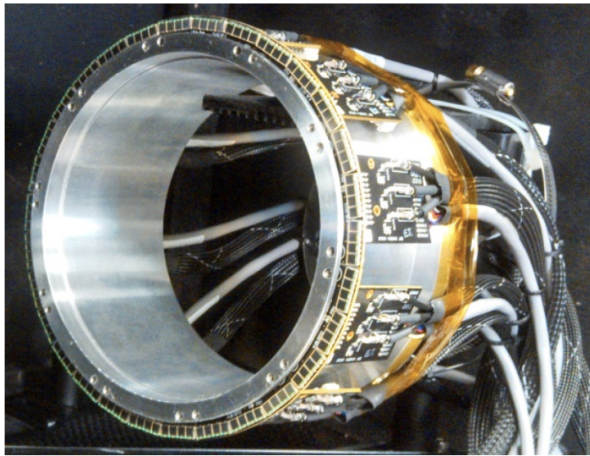


Figure 8: Fully assembled ST readout system.

165 of pre-amplifiers, 3 buffers, and 3 factor five amplifiers. Furthermore, it has 3 bias distribution channels with individual temperature compensation *via*  
170 thermistors. The ST2 is attached to the ST1 *via* 90° hermaphroditic connector.

175 The third component of the readout system, the ST3 seen in Fig. 9, provides interface to the power and bias supplies. It also routes the ADC and TDC outputs as well as the thermocouple output. The ST3 connects to the ST2 *via* a signal cable assembly seen in Fig. 8 and Fig. 9. The ST3 is installed upstream of the Start Counter and next to the beam pipe.

### 3. Simulation

180 In this section, the Monte Carlo (MC) simulations that were conducted in order to better understand the performance and characteristics of scintillators machined to the nominal GLUEX Start



Figure 9: Start counter ST3 readout system.

185 Counter design are discussed. The MC studies were performed with the use of the tool-kit GEANT4 which simulates the passage of particles through matter [8]. Comparisons are made with the data observed in experiments conducted on the bench in Sec. 5.2 and with beam data in Sec. 7.

#### 3.1. Simulating a Simplified Model of the ST

190 As discussed in Sec. 2.2, the ST scintillator paddles have a unique geometry in which the nose section tapers in width as the paddles approach the beam line at the downstream end. This tapering effect results in a unique phenomenon in which the light output of the scintillator paddle begins to increase as the source moves further away from the readout detector. At first, this phenomenon is completely contrary to what one might expect. In the traditional sense when the source moves further away from the end being readout, the photons have a larger effective path length and thus, have an increased probability in being lost for detection. However, this is antithetical relative to what is observed on the bench and in Hall-D.

195 A primitive GEANT4 simulation was conducted to investigate the aforementioned phenomenon. For simplicity, only the two trapezoidal regions of a machined scintillator paddle were considered. Namely, the wide straight section and the tapered nose section which are illustrated in the GEANT4 event display seen in Fig. 10.

200 The EJ-200 scintillator material ( $\rho = 1.023 \text{ g/cc}^3$ ,  $n = 1.58$ ) [3] was simulated with only one free parameter utilized to characterize the scintillator bar *i.e.*, the reflectivity of the *G4LogicalSkinSurface*, was set to 98% so there remained some finite probability that photons could be lost in the scintillator medium. Furthermore, the SiPM readout detector was placed at

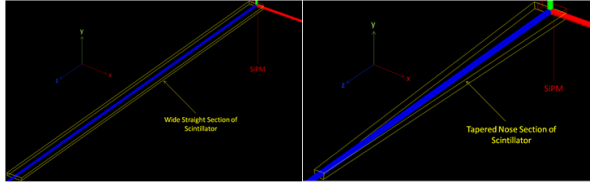


Figure 10: Simulated straight & nose section geometries. Shown is the GEANT4 event display. Left: wide straight section. Right: tapered nose section. The sections have been oriented such that they are in the same coordinate system as defined in HallD. The yellow lines are the scintillator boundaries, while the red lines are the boundaries of the SiPM.

the upstream end of the two sections, seen in Fig. 10. Moreover, the SiPM was constructed as a *G4SensitiveDetector* made of Silicon with a 100% detection efficiency. The SiPM was constructed to have an active area of  $3 \times 12 \text{ mm}^2$  which is identical to the readout system described in Sec. 2.4.

In order to simulate a charged particle traversing through the scintillator medium resulting in the production of photons along its path through the material, optical photons were generated inside the volume of the simulated scintillator material. The scintillation yield was defined to be 10,000  $\gamma$ 's/1 MeV [3]. For visual purposes, Fig. 11 shows 100 optical photons being produced at the tip of the downstream end of the two sections of the simulated scintillator paddle.

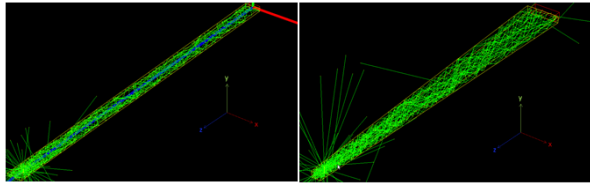


Figure 11: 100 Optical photons generated in the straight & nose sections. Left: wide straight section. Right: tapered nose section. The neon green lines are the paths of the optical photons. It is clear that some photons do in fact escape the scintillator medium, while others are collected in the simulated SiPM detector.

In order to sample the entirety of the two sections, 10,000 optical photons were generated at 16 different locations inside the medium of the scintillator. The photon energies ranged between 0.5–3.0 eV [9] and were generated randomly in  $4\pi$  along a 3 mm path ( $y - axis$ ) in the scintillator medium. The path was oriented orthogonal to the wide surface of the scintillator. In essence, this simulates

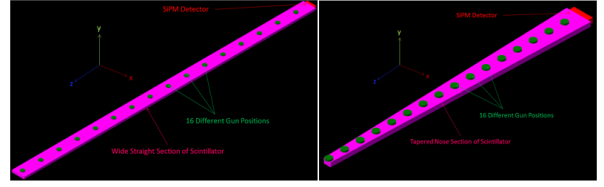


Figure 12: Optical photon gun locations along the straight & nose sections. Left: wide straight section. Right: tapered nose section. The magenta geometries indicate the scintillator boundaries of the two sections. The red box is the sensitive SiPM detector, and the green cylinders represent the location of the 16 optical photon gun locations. The locations of the source were chosen to be equal distances apart relative to each of the two sections.

a charged particle traversing through the medium with a  $\theta_{track} = 90^\circ$  in hall coordinates. The number of photons collected by the SiPM at each of the 16 source locations is counted and correlated to the source location. The results can be seen in Fig. 13. From the data it is clear that the geom-

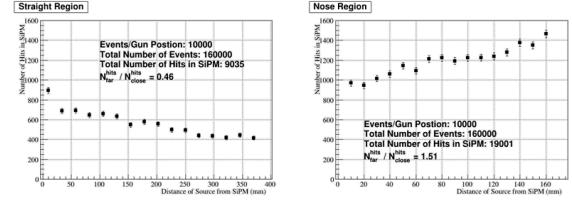


Figure 13: Simulation results for simplified two section scenario. The total number of photons which were collected by the SiPM detector at each of the 16 source locations is plotted against the sources distance from the sensitive detector. Left: wide straight section. Right: tapered nose section.

etry of the nose section results in an improvement of light collection as the source moves further away from the readout detector. In fact, there is a factor  $\approx 1/2$  light loss observed in the straight section upon comparing the number of hits collected at the closest and furthest locations relative to the readout detector. However, there is factor  $\approx 3/2$  light gain observed in the nose region. These results are primarily due to the tapering trapezoidal geometry in the nose section. This phenomenon is not observed in the quasi-rectangular straight section as it exhibits a more conventional behavior. However, this behavior in the nose region is advantageous since the majority of forward going charged particles will traverse through this region.

### 3.2. Simulating Machined Scintillator Geometry

Further simulations were conducted to simulate more realistically the effects of light collection that results from the ST scintillator geometry and optical surface quality. The ST scintillator geometry was imported into GEANT4 from a Vectorworks CAD drawing utilizing the CADMesh utility [10] and is shown via the GEANT4 event display in Fig. 14. The SiPM was constructed as a  $12 \times 12 \times 10\text{mm}^3$

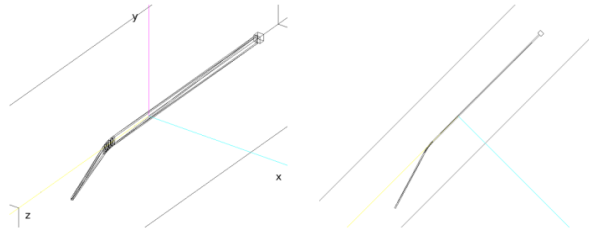


Figure 14: Scintillator geometry imported into GEANT4 utilizing the CADMesh Utility. The scintillator is coupled to a SiPM detector. Left: isometric view. Right: top view. The tapering of the nose section is clearly visible.

volume with a  $100\ \mu\text{m}$  air gap between it and the wide end of the straight section. Furthermore, the volume surrounding the scintillator volume was air. The EJ-200 scintillator material, SiPM silicon detector, and optical photons were defined in an identical manner discussed in Sec. 3.1.

To simulate the imperfections of the scintillator surfaces due to manufacturing and machining, an optical surface “skin” was defined. The “skin” material was defined to be of the type “dielectric-dielectric” and made use of the UNIFIED physics model [11] to define an imperfect scintillator surface. Both the transmission efficiency and reflection parameters were implemented as free parameters to study their various effects on light transmission.

The UNIFIED model allows one to define the finish of the scintillator surface as *polished*, *ground*, or *unified* and is illustrated in Fig. 15 [11]. In the polished model, Fresnel reflection and refraction is assumed, where as the ground model allows for Lambertian reflection, Fresnel refraction, backscattering, as well as spike and lobe reflections. The spike ( $C_{ss}$ ) reflection parameter assumes the optical photons are reflected as if the surface was a perfect mirror. The backscattering ( $C_{bs}$ ) reflection parameter assumes the photon is reflected in the same direction of incidence. The Lambertian ( $C_{dl}$ ) reflection parameter assumes that the photons are reflected corresponding to a Lambertian distribution. The lobe ( $C_{sl}$ ) reflection parameter assumes

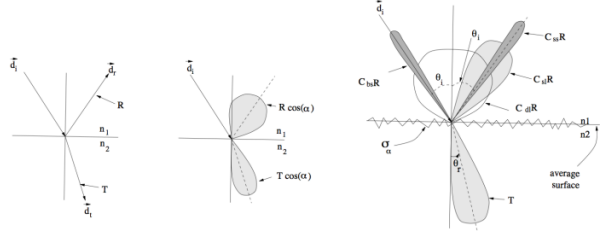


Figure 15: UNIFIED Model of scintillator surfaces. Left: Polar plot of the radiant intensity of the polished (left) and ground (right) models. Right: Polar plot of the radiant intensity in the UNIFIED model.

that the photons will reflect based on the orientation of the micro-facet on the scintillator surface, where  $\sigma_\alpha$  defines the standard deviation of the distribution of the micro-facets orientation [11]. One caveat of the aforementioned models is that they assume identical parameters for the entire optical surface [12].

As was done in section 3.1, 10,000 optical photons were generated in the scintillator medium every 2.5 cm and the number of hits collected in the SiPM were recorded. The results of these simulations are show in Fig. 16. It is clear that if the transmis-

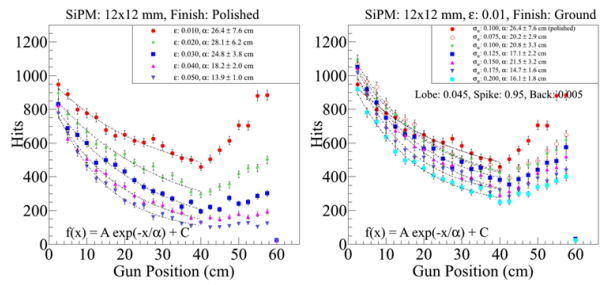


Figure 16: UNIFIED Model results. Left: polished model while varying the transmission efficiency. Right: ground model with varying  $\sigma_\alpha$  which characterizes the standard deviation of the surfaces micro-facet orientation.

sion efficiency is increased while assuming a polished surface, the amount of light collected in the SiPM also increases as illustrated in Fig. 16. Similarly, as the number of micro-facet orientations increase, meaning a more coarsely ground surface, the amount of light collection in the SiPM decreases. Moreover, in the instances where the surface quality of the machined scintillators are good, the phenomenon of light increase in the nose region as the source moves further from the readout detector is observed.

## 4. Misalignment Studies

In order to protect both the active area of the SiPMs and the scintillator surface at the upstream end, the coupling distance between the two was required to be larger than zero. Similarly, during assembly the scintillator paddles were also shimmed radially such that the top edge of the scintillator was level with the top edge of the active area of the SiPM thereby maximizing light collection. In this section we discuss the relative coupling, as well as the subsequent effects regarding light collection and time resolution, between a machined scintillator paddle and a SiPM readout detector.

### 4.1. Experimental Set-up

A custom fabricated test stand, further discussed in Sec. 5.2, and a polished scintillator machined to the nominal ST geometry, were utilized for these studies. The readout SiPM sat atop a Newport MT-XYZ (MT) compact dovetail XYZ linear translation stage[13] with three fine adjustment screws consisting of 80 threads per inch. Each knob for the three axes provides a translation of  $318 \mu\text{m}$  per rotation. For each location of the SiPM, the source and trigger PMT were located 24.5 cm downstream from the readout end.

To study the effects of the various horizontal (translations along the  $z$ -axis) coupling distances, the relative position of the active area of the SiPM and the top edge of the scintillator paddle, or vertical (translations along the  $y$ -axis) alignment, was required to be known prior too.

Utilizing an Edmund Optics complementary metal oxide semiconductor (CMOS) camera, and a reference ruler (seen in Fig. 17) the vertical alignment of the top edges of the SiPM and scintillator were measured with 0.025 mm accuracy. A micrometer was utilized in order to cross check the optical measurements and to provide absolute measurements of fixed distances in the experimental set-up. We have defined that at  $y = 0$  the SiPM and scintillator are aligned vertically. The coupling distance between the active area of the SiPM and scintillator ( $z$ ) was set to a distance of  $100 \mu\text{m}$  and monitored closely during the vertical alignment scan.

### 4.2. Vertical Alignment of SiPM & Scintillator

To measure the time resolution at various vertical alignment configurations the scintillator remained fixed while the SiPM scanned across the upstream end of the scintillator. The SiPM was lowered to

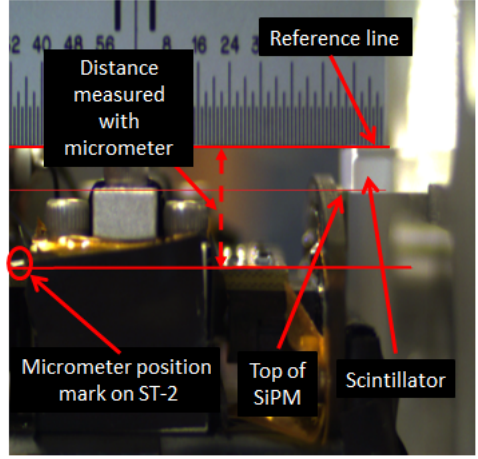


Figure 17: Vertical alignment optics set-up. The reference line corresponds to the top surface of the scintillator, while the micrometer position on the ST2 is clearly marked so that the absolute difference could be measured both optically and manually with a micrometer.

the minimum location governed by the range of the MT translation stage. This distance was measured to be  $y = -4 \text{ mm}$ .

“Coarse” measurements were then taken at half turn intervals ( $159 \mu\text{m}$ ) until the maximum height of the MT translation stage was reached which was approximately  $y = +4 \text{ mm}$ . In order to conduct “precise” measurements the SiPM was lowered to  $y = -1 \text{ mm}$  and then the translation stage was moved in quarter turn intervals ( $79.5 \mu\text{m}$ ) until it reached  $y = +1 \text{ mm}$ . The results of these measurements can be seen in Fig. 18. For each distinct

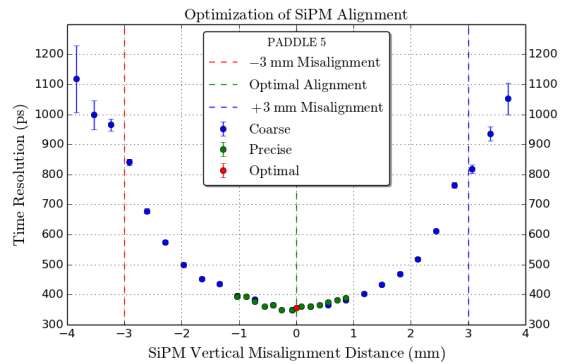


Figure 18: Coarse vertical misalignment results. The minimum time resolution obtained was approximately 350 ps which was expected. Once the SiPM exceeded  $y = \pm 3 \text{ mm}$  there is no active area of the SiPM coupled to the face of the scintillator.

location of the SiPM, the distance traversed was verified by a manual measurement made with a micrometer with  $25 \mu\text{m}$  precision.

From the vertical misalignment studies it is clear that there is no significant variation of time resolution within a  $\pm 300 \mu\text{m}$  range of the optimal alignment. These results were also simulated in a manner similar to what was discussed in section 3.2 and the results are seen in Fig. 19. The GEANT4 simu-

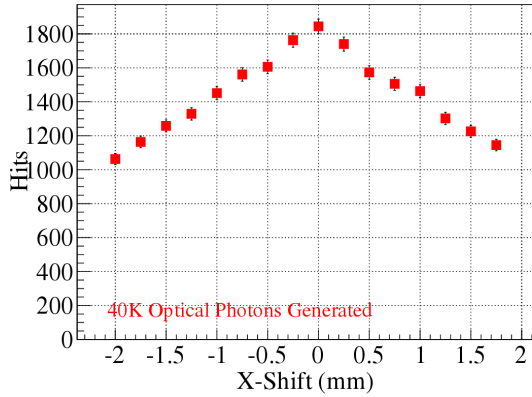


Figure 19: Vertical alignment simulation studies [14]. It is important to note the x-axis corresponds to the y-axis as discussed with the experimental measurements.

lations indicate that the acceptable range of vertical misalignment is approximately  $\pm 250 \mu\text{m}$  [14] which is consistent with what was measured on the bench.

#### 4.3. Coupling Distance of SiPM & Scintillator

With the vertical alignment between the scintillator and SiPM optimized, the effects of varying the coupling distance were also studied. Using an identical set-up as was described in section 4.2 the coupling distance, and resulting time resolutions, were measured at various locations with three distances shown in Fig. 20. While the coupling distance was

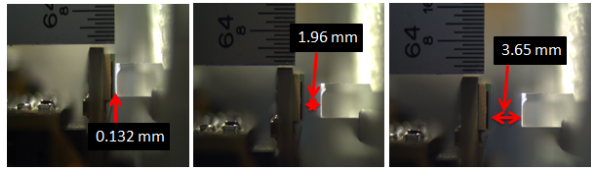


Figure 20: Various coupling distances as measured with the CMOS camera. The high degree of precision is clearly visible.

varied, the vertical alignment was kept constant at the optimal location and was monitored both optically and manually with a micrometer.

The SiPM was moved *via* the MT translation stage along the  $z$ -axis. We defined  $z = 0$  to be the instance when the active area of the SiPM was flush against the face of the machined scintillator paddle. In the coupling region  $z < 1 \text{ mm}$  the SiPM was re-ceded from the face of the SiPM in  $1/4$  turn intervals ( $79.5 \mu\text{m}$ ). For  $1 \text{ mm} < z < 2 \text{ mm}$ , the SiPM was re-ceded from the face of the SiPM in  $1/2$  turn intervals ( $159 \mu\text{m}$ ), and for  $2 \text{ mm} < z < 4 \text{ mm}$  data were collected in 1 turn intervals ( $318 \mu\text{m}$ ) with the results being illustrated in Fig. 21.

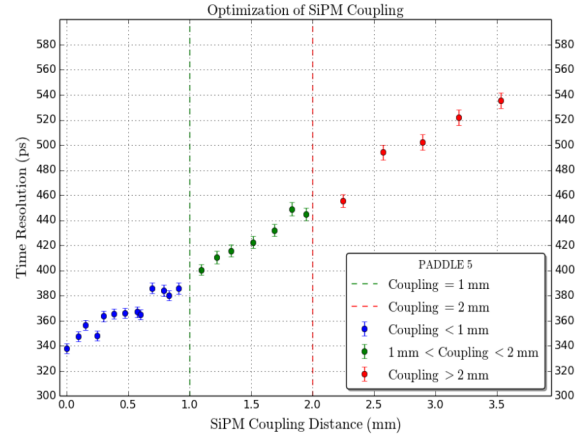


Figure 21: Coarse coupling distance studies. It is useful to note that at a coupling distance of  $251 \mu\text{m}$  the time resolution was identical to what was measured in Fig. 18 while conducting the vertical alignment studies.

It is clear from the data the optimal coupling range was  $50 \mu\text{m} < z < 350 \mu\text{m}$  and there was no significant reduction in time resolution performance over a  $0 \mu\text{m} < z < 600 \mu\text{m}$  range. Similarly, the simulation results seen in Fig. 22 also indicate that there is no significant reduction in light collection in the  $0 \mu\text{m} < z < 600 \mu\text{m}$  range [14].

## 5. Fabrication

In order to successfully identify the 2 ns electron beam bunch structure delivered by the CEBAF to within 99% accuracy, the GLUEX Start Counter time resolution is required to be  $< 350 \text{ ps}$ . In the following section the details of polishing and characterizing machined scintillators, as well as the construction of the Start Counter are discussed.

### 5.1. Polishing Machined Scintillators

The surfaces of the machined scintillators incurred a plethora of surface defects and chemical

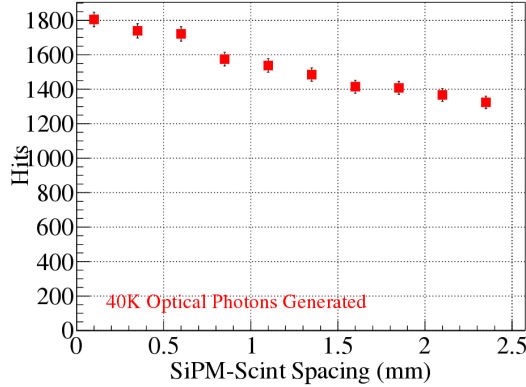


Figure 22: Coupling distance simulations. Simulations indicated that the optimal coupling distance is in the  $50 \mu\text{m} < z < 350 \mu\text{m}$  range.

contaminants known to harm scintillator surfaces while undergoing edge polishing at McNeil Enterprises. Therefore, in an effort to recover the scintillator surfaces and performance capabilities, polishing was required.

Prior to polishing the machined scintillators, a coarse measurement of the paddles performance was conducted to understand the magnitude of damage the paddles had incurred, relative to prototypes, as a result of mishandling. The time resolution and light output was measured at three precise locations along the length of the scintillators. One measurement was taken in the middle of the straight section, one in the middle of the bend, and one at the tip of the nose.

Figure 23 illustrates the erratic fluctuation and poor performance that existed from paddle to paddle prior to polishing. On average the 50 paddles did not meet the design resolution of 350 ps.

To polish the machined scintillator surfaces, Buehler Micropolish II deagglomerated  $0.3 \mu\text{m}$  alumina suspension was utilized [15]. The polishing suspension was diluted with a 5:1 ratio of de-ionized  $\text{H}_2\text{O}$  to alumina and applied to a cold, wet  $6'' \times 0.5''$  Caswell Canton flannel buffering wheel [16] operated at  $< 1500$  RPMs. All surfaces of the scintillators were carefully buffed until all large, uniform surface defects were removed. In order to eliminate small, localized surface defects hand polishing with a soft NOVUS premium Polish Mate microfilament cloth [17] and diluted polishing suspension was applied. These polishing procedures made the scintillators void of virtually all scratches and surface defects.

Once the appropriate polishing procedures had

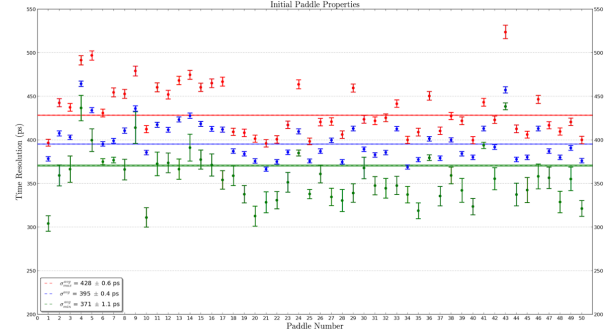


Figure 23: Coarse time resolution measurements prior to polishing. Paddle number is on the x-axis and time resolution in ns is on the y-axis. The red points are the resolutions in the bend region, the blue points are the weighted average of the three measurements, and the green points are the resolutions at the tip of the nose. The horizontal lines are the weighted averages of the individual measurements.

been developed and implemented the surface quality was greatly improved as can be seen in Fig. 24 which illustrates the same scintillator paddle before and after polishing. A red laser beam was shone

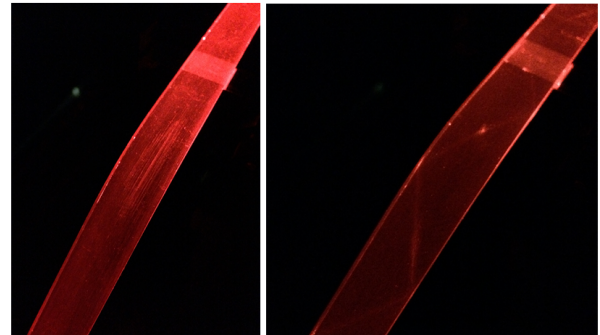


Figure 24: Effects of polishing scintillators. Left: non-diffuse laser incident on an edge, before polishing, at the upstream end of the straight section. Right: non-diffuse laser incident on the same edge, after polishing, at the upstream end of the straight section.

into the scintillator medium from the upstream end aimed at one edge so that the total internal reflection towards the tip of the nose was visible. The unpolished scintillator had such poor surface quality that the reflections in the bend region could not be seen due to the multiple scattering of light at the scintillator boundaries. However, the reflections in the polished scintillator can clearly be seen traversing down through the nose region.

Once the scintillators were polished, their performance was remeasured so that a quantitative measure of the polishing effects were understood. The

measurements were performed in an identical manner outlined above and the pre-polished results were illustrated in Fig. 23. As expected, the time resolutions were greatly improved as seen in Fig. 25. On average, at the tip of the nose, the scintillators

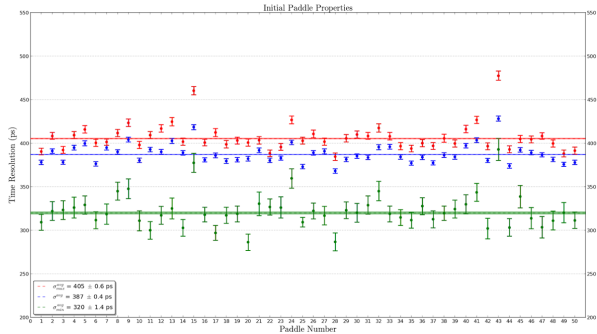


Figure 25: Coarse time resolution measurements after polishing. The details are identical to Fig. 23

exhibited a  $\approx 15\%$  improvement in time resolution. Moreover, there was a substantial reduction in erratic fluctuations in performance.

## 5.2. Testing Machined Scintillators

The polished machined scintillators were tested in order to measure their light output and time resolution properties. They were measured in an identical and reproducible manner utilizing a custom fabricated test stand shown in Fig. 26. The test

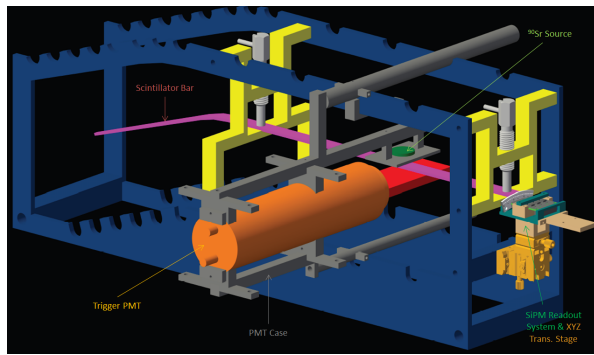


Figure 26: CAD Drawing of custom test stand.

stand facilitated the precise measurement of the aforementioned scintillator properties at 12 well-defined locations along the length of the scintillator paddles. Specifically 4 locations in the straight section, 3 in the bend, and 5 in the nose were tested.

The measurements were conducted with a collimated  $^{90}\text{Sr}$  source oriented orthogonal to the wide

flat surface of the scintillators. The  $^{90}\text{Sr}$  source provided minimum ionizing electrons ranging in energy from 0.5 – 2.3 MeV via beta-decay [18][19]. A trigger photo-multiplier tube (PMT) was placed underneath the scintillator on the opposite side of the  $^{90}\text{Sr}$  source and provided the TDC start time and ADC gate. A prototype SiPM detector identical to the SiPMs installed in the final ST assembly, was utilized to collect the light from the scintillators.

The analog signals from the SiPM and the trigger PMT were then processed through nuclear instrumentation modules (NIM) so that both the ADC and TDC spectra could be analyzed. The signal processing electronics diagram is illustrated in Fig. 27.

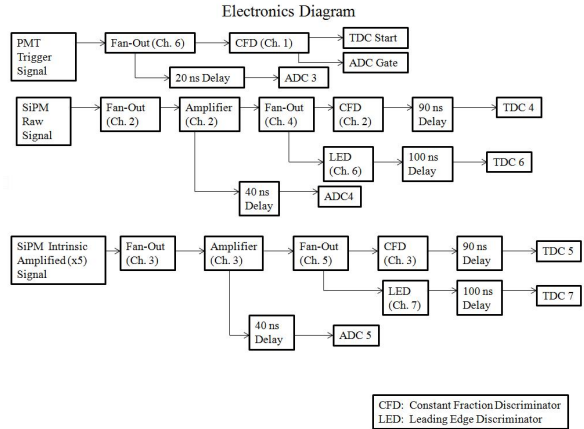


Figure 27: Electronics diagram for testing machined scintillators.

Utilizing a dedicated data acquisition computer configured with CEBAF on-line data acquisition (CODA) software, 10,000 event triggers and associated data were collected at each of the locations along the scintillator path. Subsequently, the ADC and TDC data were analyzed to measure the light output and time resolutions respectively of the whole lot of polished machined scintillators.

Once the 30 machined scintillator paddles which exhibited the best time resolution and light output properties from the lot of 50 were selected, they were carefully wrapped in Reynolds food grade aluminum foil. The aluminum foil is  $16.5 \mu\text{m}$  thick and possesses good reflectivity properties. Moreover, the aluminum foil protects the surfaces of the scintillators during both the testing and assembly processes.

The measured time resolutions for the 30 best scintillators, which comprise the ST, were found

to be satisfactory and even well below design resolution in the nose region which is illustrated in Fig. 28.

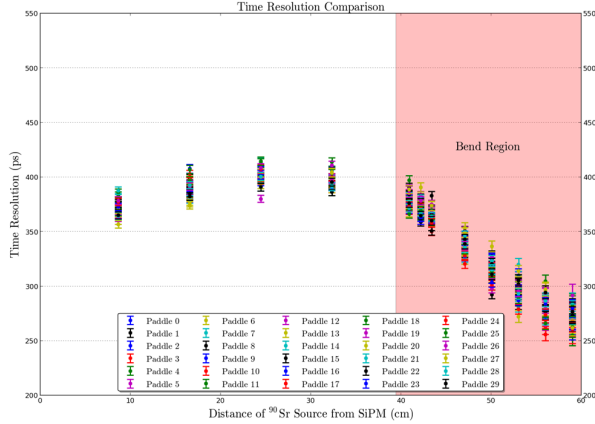


Figure 28: Time resolution of 30 the best scintillator paddles. The time resolution performance of the selected scintillators is remarkably similar while illustrating a spread of  $\approx 50$  ps in the nose region.

The unique geometry of the machined scintillator paddles exhibit a phenomenon of an increase in light collection in the nose region as the light source moves towards the tip at the downstream end. It is hypothesized that the relatively poor time resolution in the straight section is due to a reflective smearing effect in which light is able to traverse from the straight section down to the tip of the nose, and then back up to the upstream end.

The average time resolution of the individual scintillators selected for the final ST assembly are shown in Fig. 29.

### 5.3. Assembly

In order to assemble the ST an assembly jig, illustrated in Fig 30, was fabricated. The jig consisted of a rotating cylindrical mounting bracket rigidly attached to a 2" diameter shaft housed in two cast iron mounted steel ball bearings. The rotating bracket was engineered such that it was free to rotate unless engaged by a spring loaded locking plunger which would cause the assembly jig to move in discretized 12° intervals. This provided the ability to orient paddles parallel to the table top so that alignment and coupling could be performed reliably and reproducibly.

While mounted to the assembly jig, the upstream chassis (and Rohacell) was attached to the rotating bracket. A vertical bar running parallel to the table above the Rohacell served as a mount for the

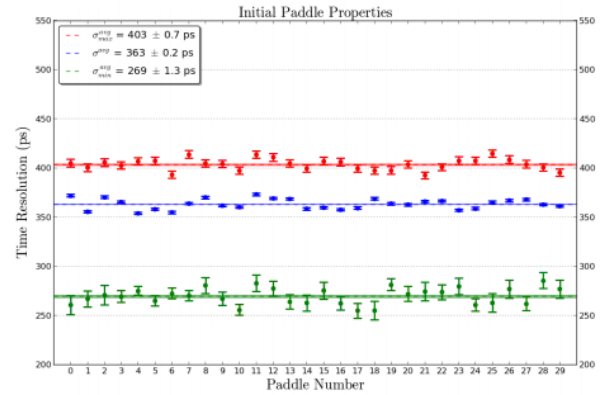


Figure 29: Average time resolution of 30 best scintillator paddles. The red data points correspond to the maximum time resolution obtained in all 12 data points. The blue data points are the weighted average of all 12 data points. The green data points indicate the minimum time resolution obtained in all 12 data points.

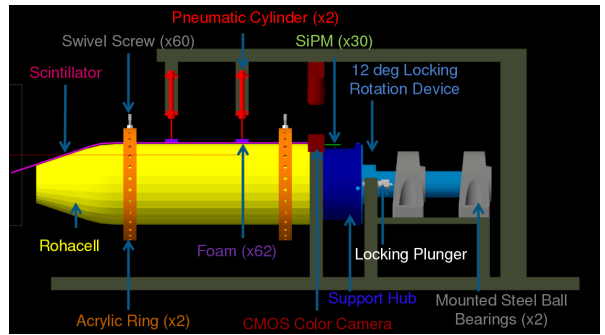


Figure 30: CAD drawing of the ST assembly jig.

pneumatic cylinders so that the scintillators could be held firmly in place during installation. Furthermore, it provided a surface in which a portable flex arm could hold the CMOS camera to monitor the coupling of the scintillators and SiPMs.

A pressurized gas system was implemented to provide manual control of the two pneumatic cylinders with soft, semi-dense rubber feet attached to the ends. The rubber feet would hold the scintillator being installed firmly in place by activating two switches which controlled each pneumatic cylinder independently via bi-directional solenoids connected in a 5 psi nitrogen gas system.

Two free floating acrylic rings, with 30 tapped holes 12° apart, were fabricated so as to firmly hold the scintillator paddles in place during assembly. Each tapped hole housed a 10° swivel pad thumb screw which had silicone foam foot ( $0.25 \times 0.25$  in $^2$ ) adhered to it in order to provide a soft barrier be-

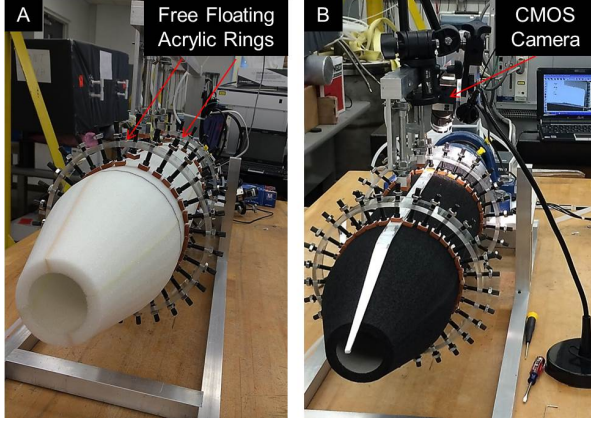


Figure 31: Free floating acrylic rings. Left: Rohacell prior to being painted with black latex paint. Each free floating ring is supported by 30 swivel pad screws. Right: Rohacell after being painted black. One wrapped scintillator paddle is being held firmly in place by two swivel pad screws.

595 tween swivel pad and the scintillator surface.

The camera and its associated software were utilized to measure scintillator/SiPM coupling distances and shimming heights with a precision of  $< 10 \mu\text{m}$  in real time. The camera was calibrated such that at various magnification settings the distance to pixel ratio was known. The 10 ST1 boards were mounted to the pre-fixed tapped holes along the lip of the upstream support hub. Black 1 mm spacers were installed between the ST1 PCB and the support hub to avoid any possibility of the electrical contact between the two. The position of the ST1 was adjusted such that the distance between the top edge of the scintillator and the top edge of the active area of the SiPM was offset by 30 mils (762  $\mu\text{m}$ ). The offset was measured with the CMOS camera.

The paddle being installed was carefully positioned such that the upstream end was located approximately a millimeter away (downstream) from the active area of the SiPM and were held in place. A piece of 0.8 mil bundling wrap was wrapped firmly around the scintillator and the Rohacell structure as seen in Fig. 32. The distance between the top edge of the scintillator and the top edge of the active area of the SiPM was then measured in order to determine the amount of shimming necessary for radial alignment as illustrated in Fig. 33. Three different thickness's (5, 10, 20 mil) of Kapton polyimide heavy duty film (type HN,  $\rho = 1.42 \text{ g/cm}^3$ ) were cut into  $0.5 \times 12 \text{ in}^2$  strips and utilized for shimming the scintillators in

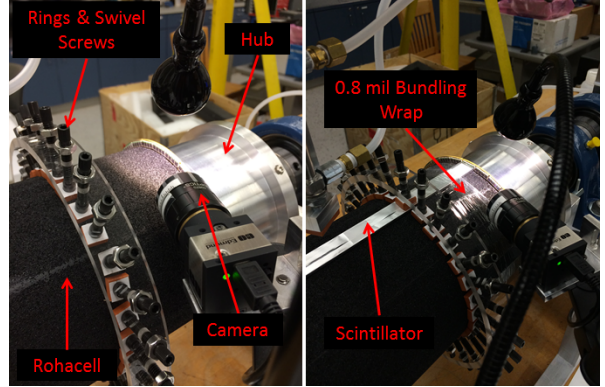


Figure 32: Aligning ST1 to support hub. Left: CMOS camera and lamp prepared to monitor ST1 positioning. Right: Reference scintillator wrapped to Rohacell during ST1 alignment.

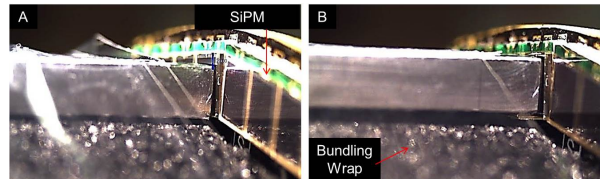


Figure 33: Shimming effects. Left: Before and Right: after shimming.

the radial direction. On average, each paddle required 30 mils of radial shimming.

With the appropriate shimming in place, the paddle was carefully positioned such that the center of the upstream paddle was aligned with the center of the SiPM and the swivel screws were extended. A piece of computer paper sandwiched between two pieces of Al foil ( $\approx 150 \mu\text{m}$  thick) was then placed parallel to the active are of the SiPM and the paddle was then pressed firmly against the outer most piece of Al foil which is seen in Fig. 34. The piece

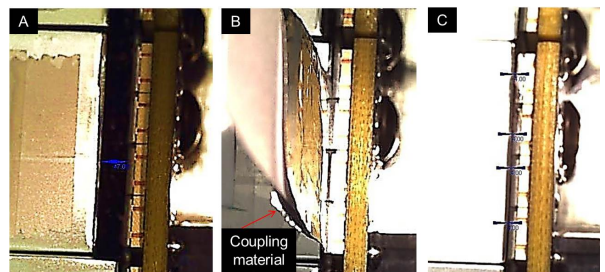


Figure 34: Steps of coupling paddles to SiPM. Left: Paddle prior to being coupled to SiPM. Center: Paddle pressed firmly against spacing material and SiPM. Right: Paddle properly coupled to SiPM at a distance of 162  $\mu\text{m}$ .

of computer paper was carefully removed. Then, the Al foil pieces were removed individually so as to ensure no damage was incurred on the paddle surface or SiPM. Utilizing this method provided a coupling distance  $< 200 \mu\text{m}$ .

In order to make the ST light tight, an inner cone of black Tedlar polyvinyl fluoride  $\rho \approx 1.5 \text{ g/cm}^3$  [20] was taped to the Rohacell as seen in Fig. 35. A

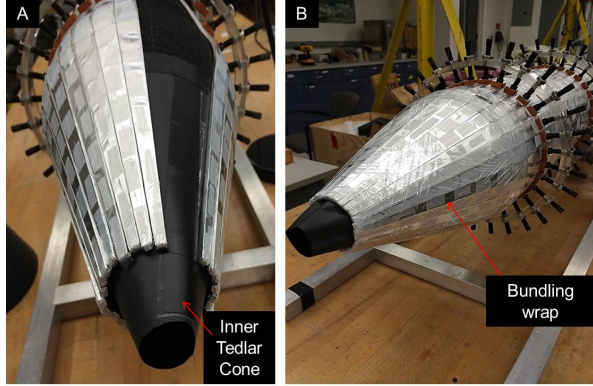


Figure 35: Inner Tedlar cone. Shown is before and after wrapping with bundling wrap. The cone was specifically engineered to have the same dimensions of the Rohacell support structure to avoid crumpling of the light tightening material.

few gaps existed in the Rohacell at the glue joints, and were filled in with black RTV silicone caulking. Moreover, it was painted with black latex paint for light tightening purposes. The support hub was also wrapped with Tedlar and taped down with black electrical tape. The spacing between the ST1 PCBs along with the bottom side of the support hub, was filled with RTV black opaque silicone caulking. Similarly, RTV silicone caulking was then applied to the inner edge of the collar which encompassed the ST1 PCBs at their outer diameter.

In order to secure paddles to the Rohacell support structure the Start Counter was wrapped along its length using self-adhesive transparent bundling wrap (0.8 mil thick, 6 in wide) at six different locations perpendicular to the central axis of rotation. Four locations were wrapped along the straight section at equal distance ( $\approx 8 \text{ cm}$ ) from one another, one in the bend and one in the nose section. Five layers of bundling wrap were applied to each section and the acrylic rings were removed as illustrated in Fig. 36.

A cone of Tedlar was wrapped around the nose region and taped down with electrical tape as seen

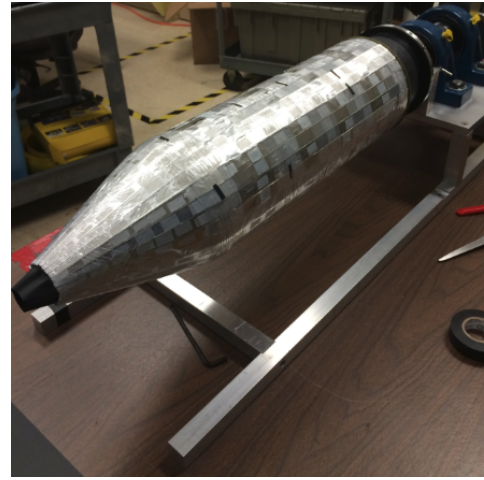


Figure 36: Isometric view of assembled Start Counter. The pieces are black electrical tape which mark the ends of bundling wrap are clearly visible.

in Fig. 37. The tips of the inner and outer cones in

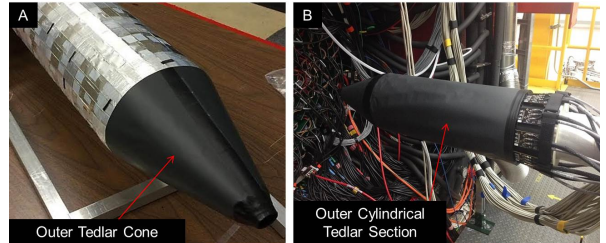


Figure 37: Light tight Start Counter. Left: Outer cone Tedlar piece. Right: Fully light tight Start Counter mounted to the Fall 2015 commissioning target.

the nose region were then taped together with electrical tape and trimmed of excess material. Furthermore, a cylindrical piece of Tedlar was taped down at the bend region and to the collar covering the ST1 boards. The fully assembled and cabled ST mounted to the commissioning target can be seen in Fig. 37.

## 6. Calibration

In this section the various calibration procedures taken in order to minimize the time resolution and enhance both the particle identification (PID) and time of flight (TOF) capabilities of the Start Counter are discussed.

### 6.1. Time-walk Correction

The time-walk effect is a well understood consequence of leading edge discriminators (LED). Analog signals of varying amplitudes crossing a fixed threshold, as determined by the discriminator threshold setting, will do so at varying times as illustrated in Fig. 38. Thus, the corresponding

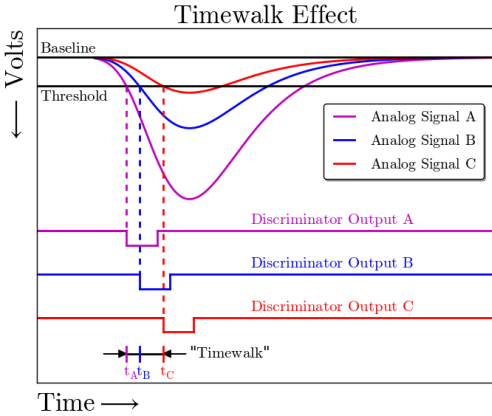


Figure 38: Example of the time-walk effect. Three coincident analog signals A, B, & C of varying amplitudes crossing a fixed threshold in a LED. The discriminator logic output signals vary in time relative to the amplitude of the incoming analog signal. The signals shown above are simulated analog signals being fed into the LED's thus, they have negative polarity.

logic signal output from the LED will “walk about” in time, resulting in an undesirable smearing of the measured ST TDC times.

The FADC250’s provide a high resolution pulse time (62.5 ps) that is time-walk independent [1] [21]. Therefore, for events in which both the FADC and TDC register hits in the same channel, the pulse time can serve as a reference time for that event. The TDC/FADC time difference is given by Eq. 1.

$$\delta t_i = t_i^{TDC} - t_i^{FADC} \quad (1)$$

Figure 39 shows a typical time-walk spectrum, *i.e.*  $\delta t_i$  versus the pulse amplitude, for one sector of the ST. The FADC250’s return both the amplitude and integral of events which are above threshold [21]. Since the amplitude better characterizes the rise time of the ADC pulse profile as compared to the pulse integral, naturally it was selected for the time-walk corrections.

From Fig. 39 it is immediately obvious that there exists a correlation between the reference time subtracted TDC time and the pedestal subtracted

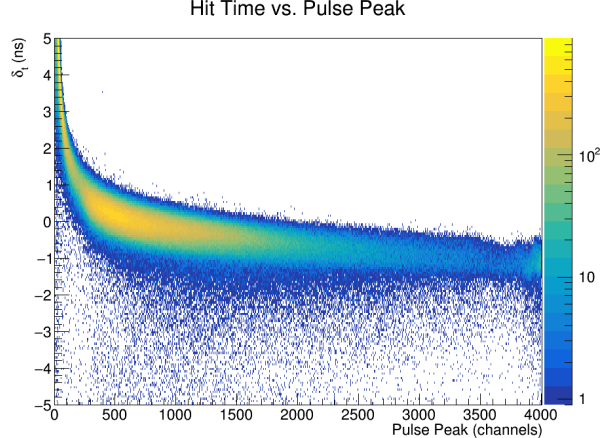


Figure 39: Typical Start Counter time-walk spectrum. Shown is the time-walk spectrum for sector 15 of the Start Counter during the Spring 2017 run. On the y-axis is  $\delta t_{15}$  and on the x-axis is the corresponding pedestal subtracted pulse peak spectrum. From this histogram it is clear that there is a correlation between the amplitude of the analog signal and the time in which the signal crosses the discriminator threshold.

pulse amplitude for hits in the ST. This correlation is nonlinear and requires a polynomial functional form to describe the correlation. Equation 2 from Ref. [22] was chosen to characterize the correlation between  $\delta t_i$  and the amplitude of the signal.

$$f_i^w(a/a_i^{thresh}) = c0_i + \frac{c1_i}{(a/a_i^{thresh})^{c2_i}} \quad (2)$$

In Eq. 2  $f_i^w$  is the functional form of time-walk fit for the  $i^{th}$  sector, while  $a$  and  $a_i^{thresh}$  are the pulse amplitude and discriminator threshold converted to ADC units respectively. Furthermore,  $c0_i, c1_i, c2_i$  are the time-walk correction fit parameters.

The data in Fig. 39 were fit using Eq. 2 and ROOT’s MINUIT  $\chi^2$  minimization fitting library [23] for pulse peak values ranging from [50, 2100]. An identical fit was carried out for each of the ST sectors.

The most probable value (MPV) of the minimum ionizing peak was chosen to be the location in which the time-walk correction was zero. This location effectively serves as a reference point for the correction. As seen in Fig. 40 a “pseudo” MPV was utilized. The “pseudo” MPV ( $a_i^0$ ) was determined on a sector by sector basis by simply acquiring the pulse peak channel which had the most number of entries after the pulse peak channel 200. The large spike in the pulse peak spectrum at very low pulse peak values are due to electromagnetic background events

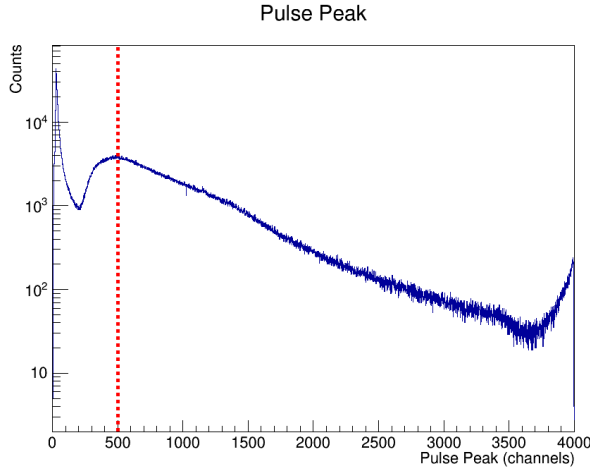


Figure 40: Typical pulse peak minimum ionizing distribution. Shown is the pulse peak minimum ionizing distribution for sector 3 during the Spring 2017 run. The red, vertical, dashed line in the histogram corresponds to the “pseudo” MPV ( $a_{15}^0$ ) which was determined to be 500.

740 clipping threshold and do not correspond to a true minimum ionizing particle traversing the scintillator medium.

Once the necessary time-walk correction parameters are determined, the correction is applied to the  
745 TDC time and is illustrated by Eq. 3.

$$T_i^w = t_i^{TDC} - f_i^w(a/a_i^{thresh}) + f_i^w(a_i^0/a_i^{thresh}) \quad (3)$$

With the time walk corrections having been applied, the corrected timing distributions appear much more uniform in nature and exhibit a factor 1.75 improvement in resolution [1]. Figure 41 illustrates the vast improvement in the time difference spectrum ( $\delta t_{15}$ ) due to the applied time-walk corrections. Figure 42 illustrates the  $\delta t_{15}$  distribution and the relative effects of the aforementioned  
750 time-walk correction.

## 6.2. Propagation Time Corrections

As a charged particle traverses through the ST  
755 scintillator material the molecules become excited and a small fraction ( $\approx 3\%$ ) [24] of the excitation energy is released in the form of “optical” photons. The photons produced will be emitted uniformly in all directions and some will escape the medium, some will be reflected back into the medium by virtue of the reflective Al foil wrapping, and some will be lost. However, the photons which are in fact not lost, will totally internally reflect until

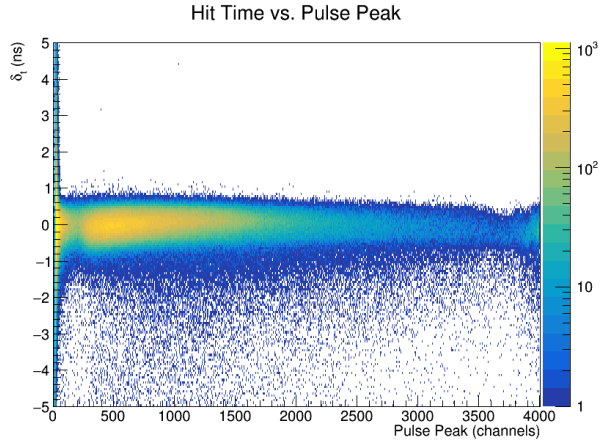


Figure 41: Time-walk corrected time difference spectrum. Shown is the time-walk corrected time difference spectrum for sector 3 during the Spring 2017 run. The time-walk corrected time difference spectrum has  $\sigma_{\delta t_{15}} \approx 270\text{ps}$

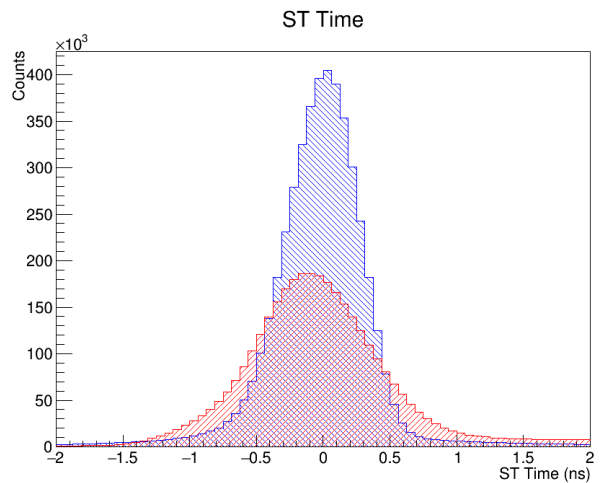


Figure 42: Comparison of pre and post self-timing distributions.

they reach the SiPM detector placed at the upstream end. The moment the photons are produced they will begin to propagate through the scintillator medium until they are eventually detected. The time from production to the time of detection in the ST scintillator paddles must be accounted for and is discussed below.

The EJ-200 scintillator material has a refractive index equal to 1.58 [3] meaning that light in the medium will travel with a velocity  $\approx 19\text{ cm/ns}$ . However, what is measured in the lab is known as the effective velocity which is slower due to the fact that the majority of photons are not traveling in

780 straight lines parallel to the medium boundaries. Instead they are constantly reflecting off the boundaries resulting in an increase in their respective path lengths which contributes to an observed reduction in velocity. This velocity is known as the effective  
 785 velocity.

Correcting for the time in which light spends traversing through the scintillator material is a necessary correction since the ST paddles are 60 cm in length. Thus, light produced in the tip of the nose  
 790 will take on the order of 4 ns to reach the SiPM at the upstream end. Performing the propagation time corrections utilizing the common effective velocity method is not the most robust procedure for the case of the ST. Studies performed with simulation  
 795 and data showed that the unique geometry in the nose causes the effective velocity of light to be larger than that of the straight section and therefore they must be treated in an independent manner.

In order to conduct the propagation time corrections for the ST a distinct set of events needed to be selected so that a well defined reference time was being utilized. This reference time was utilized as a measure of the event time for all other charged tracks intersecting the ST within the same event.  
 800

For every charged track in a given event, two global tracking requirements were required. First, only charged tracks with a tracking confidence level, or tracking figure of merit (FOM), greater than 0.0027 were considered. Secondly all charged tracks  
 805 were required to have the  $z$  coordinate of its vertex to be contained with in the target geometry *i.e.*  $50.0 \text{ cm} < z_{\text{vertex}} < 80.0 \text{ cm}$ . Moreover, the  $r$  coordinate of the tracks vertex was required to be contained within the target radius *i.e.*  $r_{\text{vertex}} = \sqrt{x_{\text{vertex}}^2 + y_{\text{vertex}}^2} < 1 \text{ cm}$ . Only tracks passing these fiducial cuts were considered for analysis.  
 810

Two specific tracks were required in each event in order to conduct the ST propagation time corrections. One track that has a match to the time of flight (TOF) detector and not the ST provides the reference time for that event. A separate track that has a match the ST and not the TOF was used to provide the ST measure of the vertex time. This was done in order to avoid any potential bias in the calibration.  
 815

The advantage of using the time associated with a track matched to the TOF is that the time resolution of the TOF is the best of any detector in Hall-D ( $\approx 96 \text{ ps}$ ) [25]. The calibrated (time-walk &  
 820 propagation) hit time returned by the TOF ( $T_{\text{hit}}^{\text{TOF}}$ ) was then corrected for the flight time from the track  
 825

vertex to the TOF ( $T_{\text{flight}}^{\text{TOF}}$ ). Equation 4 is the TOF measure of the track vertex time.

$$T_{\text{vertex}}^{\text{TOF}} = T_{\text{hit}}^{\text{TOF}} - T_{\text{flight}}^{\text{TOF}} \quad (4)$$

In order to determine the time in which the beam bunch arrived at the interaction point ( $T_{\text{vertex}}^{\text{BB}}$ ) the  $T_{\text{vertex}}^{\text{TOF}}$  time must first be corrected for the RF measure of the vertex time ( $T_{\text{vertex}}^{\text{RF}}$ ). The RF signal that is readout in Hall-D is provided by the CE-BAF accelerator at a rate of 499 MHz (2.004 ns) while the beam bunches are produced at a rate of 249.5 MHz (4.008 ns). The RF signal from the accelerator is multiplexed into TDC's however, the provided signal rate is too high to readout without causing overflow in the TDC buffers thus the RF signal is pre-scaled [26]. The pre-scale factor was 128 and consequently the RF signal was readout every  $128 \times 2.004 \text{ ns} = 256.512 \text{ ns}$ . Thus, the time associated with the beam bucket that produced the event of interest must be calculated since it is not provided directly.

For every event, the associated RF time is the pre-scaled time the RF signal arrived at the center of the target ( $T_{\text{center}}^{\text{RF}}$ ). This time must be propagated out to the vertex location of the track since the photon responsible for the track spends a non-negligible finite amount of time traversing through the target before interacting with it. This propagation time ( $T_{\text{prop}}^{\text{RF}}$ ) correction is given by Eq. 5

$$T_{\text{prop}}^{\text{RF}} = (z_{\text{vertex}} - z_{\text{center}}^{\text{target}}) \cdot \frac{1}{c} \quad (5)$$

Once the propagation time is summed with the centered RF time ( $T_{\text{center}}^{\text{RF}}$ ) one obtains the measure of the RF time at the vertex of the track and is given by Eq. 6.

$$T_{\text{vertex}}^{\text{RF}} = T_{\text{center}}^{\text{RF}} + T_{\text{prop}}^{\text{RF}} \quad (6)$$

Due to the inherent ambiguity associated with pre-scaling,  $T_{\text{vertex}}^{\text{RF}}$  is not the correct measurement of the time the beam bunch actually produced the track. Therefore, one must "step"  $T_{\text{vertex}}^{\text{RF}}$  to the time the track was produced as measured by  $T_{\text{vertex}}^{\text{TOF}}$ . To do this one must first calculate the time difference  $\delta T$  given by Eq. 7.

$$\delta T = T_{\text{vertex}}^{\text{TOF}} - T_{\text{vertex}}^{\text{RF}} \quad (7)$$

Next, one must calculate the number of beam buckets ( $N_{\text{step}}^{\text{buckets}}$ ) that have elapsed during the  $\delta T$  time

period and is given by Eq. 8, where ( $N_{step}^{buckets}$ ) is rounded to the nearest integer.

$$N_{step}^{buckets} = \frac{\delta T}{T_{period}^{BB}} = \frac{\delta T}{4.008 \text{ ns}} \quad (8)$$

Lastly one can now calculate the time the beam bunch arrived at the vertex that produced the track ( $T_{vertex}^{BB}$ ) and is given by Eq. 9.

$$T_{vertex}^{BB} = T_{vertex}^{RF} + T_{period}^{BB} \cdot N_{step}^{buckets} \quad (9)$$

For every event, the first track satisfying the aforementioned fiducial track selection and is matched to the TOF will then have the associated  $T_{vertex}^{BB}$  time calculated. This time serves as the reference time for all other tracks that have intersected the ST in that event.

In order to properly calculate the propagation time ( $T_{prop}^{ST}$ ) of photons produced by a charged track intersecting the ST, a few quantities must be known. Particularly the time-walk corrected hit time ( $T_{hit}^{ST}$ ), the flight time from the track vertex to the ST intersection point ( $T_{flight}^{ST}$ ), and a well defined reference time corresponding to the event ( $T_{vertex}^{BB}$ ). With the reference time determined, all other charged tracks passing the previously discussed fiducial track selection and which have a match to the ST (and not the TOF) are analyzed. Equation 10 illustrates the ST measure of the vertex time.

$$T_{prop}^{ST} = T_{hit}^{ST} - T_{flight}^{ST} - T_{vertex}^{BB} \quad (10)$$

This time difference is a direct measure of the amount of time the detected light produced by the intersecting charged track spent traversing the scintillator medium. In order to perform the propagation time corrections the  $z$ -coordinate of the tracks intersection point with the ST ( $z_{hit}^{ST}$ ) was also recorded for every charged track intersecting the ST. Once both  $T_{prop}^{ST}$  and  $z_{hit}^{ST}$  were calculated, the propagation correction calculation could be performed. Figure 43 illustrates correlation between these two quantities.

The mean propagation times were then grouped into three distinct regions corresponding to the three unique geometrical sections of the ST namely the straight, bend, and nose regions. These three regions were then fit utilizing the  $\chi^2$  minimization technique with a linear function whose functional form is given by Eq. 11 where the index  $i$  indicates which region the fit is being performed.

$$f_i(z) = A_i + B_i \cdot z \quad (11)$$

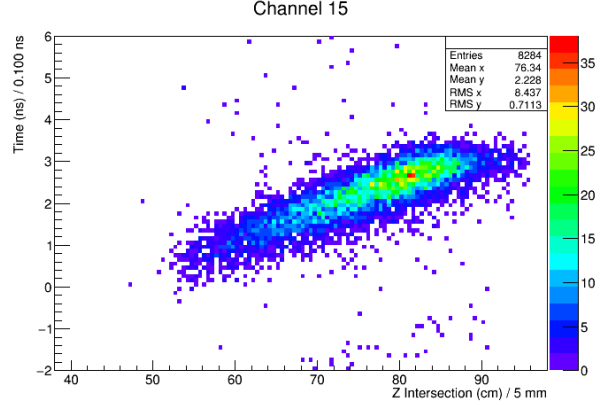


Figure 43: Typical Start Counter propagation time correlation. Shown is the ST propagation time correlation for sector 15 of the ST during the Spring 2015 run 2931.  $T_{prop}^{ST}$  is plotted on the y-axis and the  $z_{hit}^{ST}$  is plotted along the x-axis. There is a clear correlation between the time in which optical photons are detected by the SiPM and the location of the charged track intersection point with the ST.  $z$  is in hall coordinates.

The distributions and associated fits for the three regions are illustrated in Fig. 44.

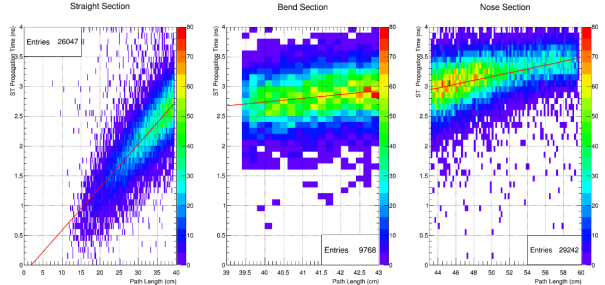


Figure 44: Typical Start Counter propagation time projection correlation. Left: Typical propagation time projection correlation for sector 15 of the ST during the Spring 2015 run 2931. The red line serves as a reference for the propagation time assuming it was a constant 15 cm/ns. The magenta line is the fit corresponding to the straight section. The green and dark blue solid lines correspond to the fits in the bend and nose section respectively. Right: zoomed in view of data points.

With the fit parameters determined an explicit time difference correction for each of the ST sectors could then be applied to calculate the ST measure of the vertex time given by Eq. 12 which must be a function of where the charged track intersects with the ST.

$$T_{vertex}^{ST}(z) = T_{hit}^{ST} - T_{flight}^{ST} - T_{prop}^{ST}(z) \quad (12)$$

Figure 45 illustrates the propagation time corrected ST time as a function of the  $z$ -intersection of

charged tracks match the the ST. In comparison to

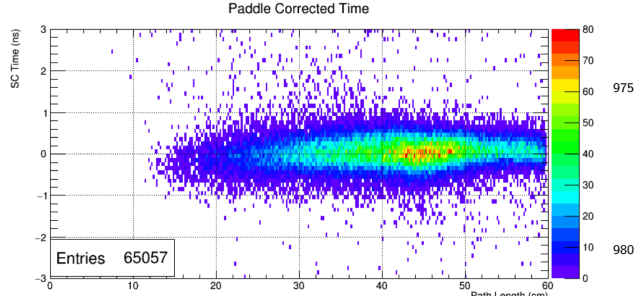


Figure 45: Calibrated ST time versus the  $z$ -intersection of charged tracks matched to the ST.

Fig. 43, Fig. 45 no longer illustrates a dependence on the where the charged track intersects with the ST paddles as expected.

After the propagation time corrections are applied the ST corrected time now measures the vertex time for the track in the event and is discussed further in Sec. 7

### 6.3. Attenuation Corrections

When photons traverse through a scintillator medium they can be lost through scattering, absorption, or escape at the boundaries. Attenuation corresponds to the reduction in observed light relative to the amount of initial scintillation light produced in the medium.

Photons produced in a scintillator medium, as a result of charged particles traversing through the material, are subject to the property of total internal reflection. If the resulting photons incident on the scintillator-air boundary have an angle of incidence which is smaller than the critical angle, then the photons will leave the scintillator medium and be lost for detection and thus contribute to the overall attenuation. However, if the incident photon has an angle of incidence which is equal to or greater than the critical angle,  $39.3^\circ$  for the ST scintillator-air interface [1], then those photons will totally internally reflect and may possibly be detected. The photons that do in fact totally internally reflect however, are still subject to additional phenomena which contribute to the overall attenuation of photons in the scintillator medium.

With the above factors considered, one can define a parameter known as the *attenuation coefficient* which characterizes a particular materials ability to absorb photons. The attenuation coefficient is defined to be the length in the medium in which the

initial number of primary photons are reduced by a factor of  $1/e$  (36.8%). Since the loss of photons in scintillators equates to the loss of information relative to the event of interest, it is desirable to have a scintillator material with a long attenuation length. For reference a flat  $2 \times 20 \times 300 \text{ cm}^3$  EJ-200 scintillator has a relatively long attenuation length on the order of 4 m [3].

The measured energy deposited ( $dE_{\text{meas}}$ ) from a charged particle traversing a scintillator medium is proportional the number of photons created, which is in turn proportional to the integrated pulse read out by the FADC250. However, since the photons created *via* ionization are subject to attenuation as they propagate through the scintillator medium, the energy deposition measured by the SiPM does not correctly measure the energy deposited by the charged particle at the location of intersection with the scintillator.

In order to obtain the attenuation coefficients of interest tracks matching to the ST, while passing identical fiducial track selection cuts as discussed in Sec. 6.2, were selected for analysis. Furthermore the tracks pedestal subtracted pulse integral, energy deposition per unit length ( $dE_{\text{meas}}/dx$ ), and  $z$ -intersection with the ST were recorded. A plot of the uncorrected energy deposition per unit length versus the track momentum ( $dE_{\text{meas}}/dx$  vs.  $p$ ) for tracks matched to the ST are shown in Fig. 46. It

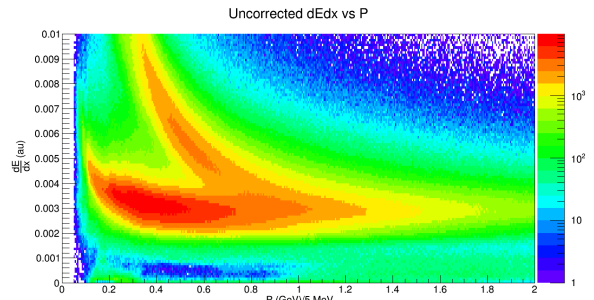


Figure 46: Typical uncorrected  $dE_{\text{meas}}/dx$  vs.  $p$  distribution in the Start Counter. Shown is the uncorrected  $dE_{\text{meas}}/dx$  vs.  $p$  distribution for tracks matched to the Start Counter in the Spring 2015 run 2931. The “banana band” corresponds to protons while the horizontal band corresponds to charged electrons, pions, and kaons.

is clear from Fig. 46 that no reliable PID can occur for tracks with  $p > 0.6 \text{ GeV}/c$ .

The pedestal corrected pulse integral data were binned in 1 cm  $z$ -intersection bins along the full length of the paddle. These data in the nose section

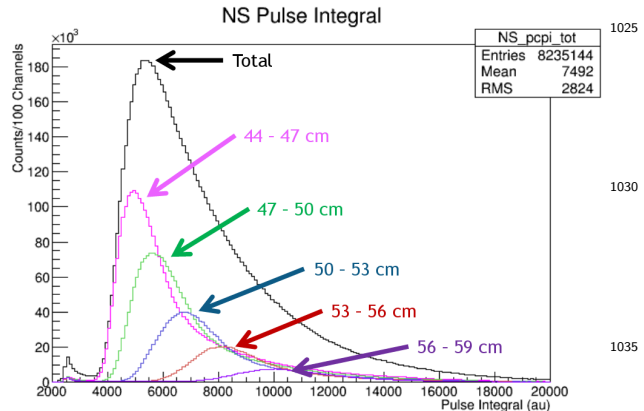


Figure 47: Pedestal subtracted FADC pulse integral spectrum corresponding to the three ST sections.

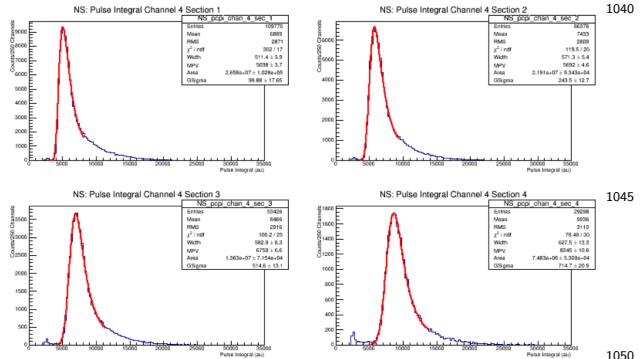


Figure 48: Vavilov fits to extract the MPV of pedestal subtracted pulse integral FADC250 data in the nose section.

are represented in Fig. 47. In order to properly quantify the pulse integral data, the most probable value (MPV) of the data was extracted utilizing the energy straggling distribution known as the Vavilov distribution [27].

The Vavilov distribution, a generalization of the Landau distribution, is often utilized to describe the corresponding energy loss of charged particles traversing a thin layer of matter [28]. Unlike the more restrictive Landau distribution, the Vavilov distribution accounts for the maximum allowable energy transfer in a collision between a particle and an atomic electron [29]. Therefore, the pulse integral data for each 1 cm bin along the length of the ST paddles were fit utilizing the Vavilov distribution and the associated MPV was extracted. The fits to the data are illustrated in Fig. 48. With the MPV values extracted for each 1 cm  $z$ -intersection bin, the MPV values are plotted against the central value for each  $z$ -intersection bin as seen in

Fig. 49. This allows for one to quantitatively measure the attenuation of photons in the ST scintillators.

As was discussed in Sec. 3.2 the unique geometry of the ST causes for the two distinct regions, *i.e* straight and nose, to have differing properties in terms of light output and thus, time resolution. Therefore, when performing attenuation corrections the two regions were treated independently in order to properly characterize photon attenuation.

It was empirically determined that the ideal fit function for the straight section would follow Eq. 13.

$$f_S(z) = A_S e^{B_S \cdot z} \quad (13)$$

Similarly, the functional form of the nose section follows Eq. 14.

$$f_N(z) = A_N e^{B_N \cdot z} + C_N \quad (14)$$

Exponential decay functions are typically used to describe the attenuations of photons in scintillator material. However, for the unique case of the nose section, an exponential growth function was utilized. In order to investigate the possibility of utilizing a single functional form to describe the entire length of a scintillator paddle, a polynomial of  $\mathcal{O}(5)$  was also studied however was deemed unsuitable at the boundary regions [1].

Figure 49 illustrates the pulse integral mean vs.  $z$ -intersection along the paddle for sectors 5 and 23. It is clear that the aforementioned exponential func-

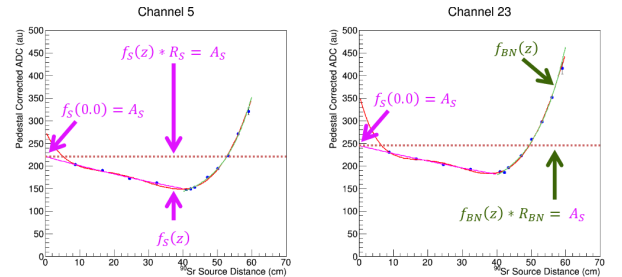


Figure 49: Two particular cases in which the polynomial of  $\mathcal{O}(5)$  fits the ADC mean data relatively well. The red line corresponds to the polynomial of  $\mathcal{O}(5)$  fit. The magenta line is the exponential fit to straight section [0 cm, 40 cm] while the green line is the exponential fit to the nose section [40 cm, 60 cm]. Sector 5 is on the left while sector 23 is on the right. The red horizontal dashed line corresponds to the value of the exponential fit in the straight section evaluated at  $z = 0$  cm.

tions, corresponding to their respective geometrical sections, fit the data in a robust manner.

Evaluating the fit function in the straight section at  $z = 0$  cm is representative of a minimum ionizing particle traversing through the upstream end closest to the SiPM readout. In this instance the detected photons traverse through virtually no scintillator material, and are thus subject to no effects of attenuation. Therefore, for all charged particles passing through the ST scintillator paddles we apply an attenuation correction to the deposited energy measurement ( $dE_{meas}$ ) to preserve the information regardless of where the track intersects the paddles. The corrected energy deposition ( $dE_{corr}$ ) is given by Eq. 15 where the index  $i$  indicates which section the charged track intersected with.

$$dE_{corr} = dE_{meas} \cdot R_i \quad (15)$$

For the straight section we have Eq. 16.

$$R_S = \frac{f_S(0.0)}{f_S(z)} = e^{-B_S \cdot z} \quad (16)$$

For the nose section we have Eq. 17.

$$R_N = \frac{f_N(0.0)}{f_N(z)} = \frac{A_N}{A_N e^{B_N \cdot z} + C_N} \quad (17) \quad 1105$$

Thus, for every hit along the length of the ST paddles we find Eq. 18 & Eq. 19.

$$f_S(z) \cdot R_S = A_S \quad (18) \quad 1110$$

$$f_N(z) \cdot R_N = A_N \quad (19)$$

Once all energy deposition measurements have had the appropriate attenuation corrections applied as was discussed above, the PID capabilities of the ST are considerably enhanced and are discussed further in Sec. 7.

## 1085 7. Performance

The ST was installed in Hall-D just prior to the Fall 2014 GLUEX commissioning run. It was not until the Spring 2015 commissioning run that enough statistics were obtained with an  $LH_2$  target to perform reliable calibrations. With the aforementioned data set, the procedures to calibrate the detector and measure its performance were developed and deployed.

As was discussed in previous sections, the geometry of the ST nose section results in an increase of the light output as the scintillation source moves towards the downstream end. While investigating FADC250 data under nominal beam conditions, this phenomenon was immediately observed

through the pulse amplitude and pulse integral data. Figure 50 illustrates that similar to the bench measurements the light output increases exponentially, as the scintillation source moves towards the downstream end. This feature of the ST geometry

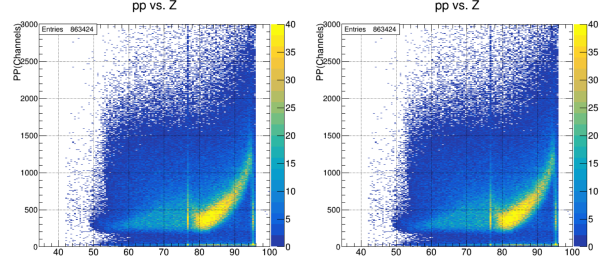


Figure 50: FADC spectra from the Spring 2017 run. Left: pulse integral versus the  $z$ -intersection of charged tracks matched to the ST. Right: pulse amplitude versus the  $z$ -intersection of charged tracks matched to the ST. The straight section corresponds to  $40 \text{ cm} < z < 80 \text{ cm}$ , the bend section  $80 \text{ cm} < z < 84 \text{ cm}$ , and the nose section  $84 \text{ cm} < z < 98 \text{ cm}$ .

is extremely advantageous since the majority of the charged tracks produced under the nominal GLUEX beam conditions intersect the ST in the nose region and therefore have the largest light amount of light collected by the SiPM's as the upstream end.

Once the proper attenuation corrections were applied to the data, the PID capabilities of the ST were greatly enhanced. Figure 51 illustrates the PID capability of charged tracks intersecting the ST. As compared to Fig. 46, the reliable separation of protons and other hadrons occurs for charged tracks with  $p < 1.1 \text{ GeV}/c$  which is a factor two improvement from the uncalibrated data.

After the previously discussed time-walk and propagation time corrections were complete, it was then possible to utilize the ST to measure the time of charged track vertices for tracks that are matched to the ST. The vertex time is defined to be the time in which a polarized Bremsstrahlung photon interacted with the  $LH_2$  target and produced a charged track that intersected the ST. An identical charged track selection process as outlined in Sec. 6.2 was utilized so that the time resolution of tracks matched to the ST could be measured.

The equation to calculate the ST measure of the vertex time is given by Eq. 10. In an identical manner outlined in Sec. 6.2,  $T_{vertex}^{RF}$  must be “stepped” to the time the charged track vertex was produced so as to obtain a proper measure of the RF time. The resulting distribution in the time difference of

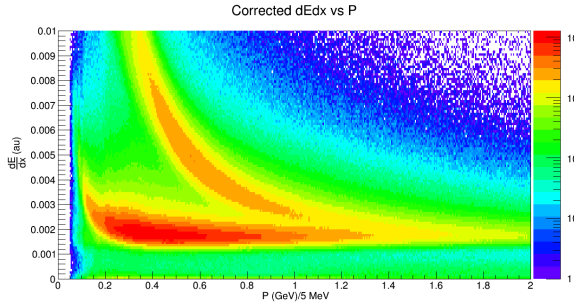
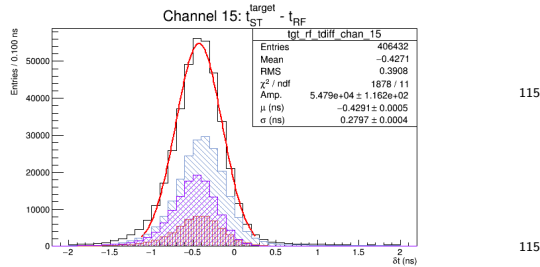


Figure 51: Typical corrected  $dE/dx$  vs.  $p$  distribution in the Start Counter. Shown is the corrected  $dE/dx$  vs.  $p$  distribution for tracks matched to the Start Counter in the Spring 2017 run. The “banana band” corresponds to protons while the horizontal band corresponds to charged electrons, pions, and kaons. It is clear that pion/proton separation is achievable for tracks with  $p < 1.1 \text{ GeV}/c$ .

1135 these two times provides a measure of the ST time resolution and is seen in Fig. 52.



1140 Figure 52: Typical Start Counter/RF time resolution distribution. Shown is the time resolution distribution for sector 1150 15 during the Spring 2015 run 2931. The x-axis is the time difference between  $T_{vertex}^{ST}$  and  $T_{vertex}^{BB}$ . The blue histogram is the resolution in the straight section. The red and purple histograms correspond to the resolution in the bend and nose sections respectively. The black histogram is a sum of the three sections and corresponds to the resolution along the entire length of the paddle.

1145 The aforementioned fits were then carried out for each of the ST sectors with  $\sigma$ , and its associated error being calculated. Then a weighted average of the 30  $\sigma$ 's were calculated so that the ST could have its time resolution characterized in its entirety. The same procedure was also conducted for the three individual sections. Figure 53 illustrates the uniformity in time resolution among all sectors of the ST.

1150 Figure 53 indicates that the average time resolution of 300 ps is well below the design resolution of 350 ps. Table 1 details the weighted average time resolution of all the ST sectors in the different geo-

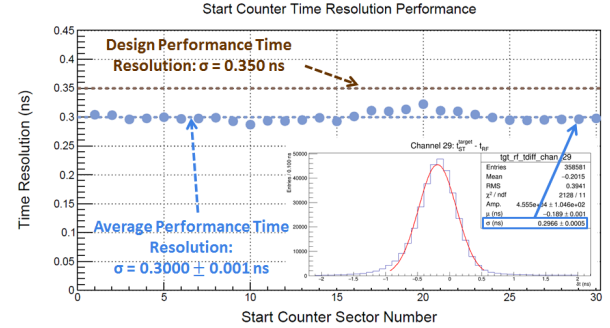


Figure 53: ST time resolutions as a function of sector number. The inset illustrates a 2  $\sigma$  Gaussian fit to the the ST time minus the RF time. The resulting  $\sigma$  of the fit provides a measure of the time resolution.

metrical regions. It is clear from Table 1 that what

Section	$\sigma_{\text{all}}$	$\sigma_{\text{straight}}$	$\sigma_{\text{bend}}$	$\sigma_{\text{nose}}$
$\sigma_{\text{avg}}$	290 ps	299 ps	292 ps	264 ps

Table 1: Average time resolutions by section. Shown is the average of all 30 ST sectors by independent geometrical regions.

is observed is that measurements made with beam data exhibit the same phenomenon of substantial improvement in light collection, and thus time resolution, as light is produced further downstream in the nose region.

When these time resolution measurements were conducted with data collected in Spring 2017, approximately 3 years had elapsed since the paddles were first tested on the bench at FIU. Prior experience with degrading scintillators indicates that degradation in time resolution will be visible in a matter of weeks. However, after 3 years no degradation has been observed and the ST is still performing well below design resolution.

## 8. Conclusion

The GLUEX Start Counter was designed and constructed at Florida International University for use in Hall-D at TJNAF to provide separation of the 500 MHz photon beam bunch structure delivered by the CEBAF to within 99% accuracy. It is the first “start counter” detector to have utilized magnetic field insensitive SiPMs as the readout system. Despite the many design and manufacturing complications, the ST has proven to have performed well beyond the design timing resolution of 350 ps

with an average measured resolution of 250 ps. Furthermore, the capabilities of the ST make it a viable candidate to assist in PID calculations.

The unique geometry of the ST nose section has illustrated the advantage of tapering trapezoidal geometry in thin scintillators. Through simulation, tests on the bench, and analysis of data obtained with beam it has been definitively demonstrated that this geometry results in a phenomenon in which the amount of light detected increases as the scintillation source moves further downstream from the readout detector.

Since it's installation in Hall-D during the Fall 2014 commissioning run, the ST has shown no measurable signs of deterioration in performance. This suggests that the ST scintillators are void of crazing and will most likely be able to meet and exceed the design performance well beyond the scheduled run periods associated with the GLUEX experiment.

It is planned to incorporate the ST into the level 1 trigger of the GLUEX experiment for high luminosity ( $> 0.5 \mu A$ ) running. Preliminary studies suggest that the high efficiency ( $> 95\%$ ) of the ST, in combination with the calorimeters, provides good suppression of electromagnetic background in regards to the level 1 trigger. Furthermore, the ST's high degree of segmentation has shown to suppress various background contributions associated with complex topologies while simultaneously providing precision timing information for reconstructed charged particles in GLUEX.

## 9. Acknowledgments

The authors would like to graciously thank the plethora of Jefferson Lab staff members in both the Engineering division and Hall-D. Their numerous and invaluable contributions allowed for the Start Counter project to come to fruition. The authors would also like to extend their gratitude to the entire GLUEX Collaboration who provided fruitful ideas and advice throughout the many stages of the project. Work at Florida International University was supported in part by the Department of Energy under contracts DEFG0299ER41065 and DE-SC0013620. Furthermore, this material is based upon work supported by the U.S. Department of Energy, Office of Science, Office of Nuclear Physics under Contract No. DE-AC05-06OR23177.

## References

- [1] E. Pooser, The GlueX start counter and beam asymmetry  $\Sigma$  in single  $\pi^0$  photoproduction, Ph.D. thesis, Florida International University (2016).
- [2] <http://www.eljentechnology.com/>.
- [3] General Purpose Plastic Scintillator EJ-200, EJ-204, EJ-208, EJ-212, technical note available at [http://www.eljentechnology.com/images/products/data\\_sheets/EJ-200\\_EJ-204\\_EJ-208\\_EJ-212.pdf](http://www.eljentechnology.com/images/products/data_sheets/EJ-200_EJ-204_EJ-208_EJ-212.pdf).
- [4] <http://www.rohacell.com>.
- [5] <http://www.mcnealplasticmachining.com/>.
- [6] <http://www.hamamatsu.com/us/en/index.html>.
- [7] Multi-Pixel Photon Counter, technical note available at [https://halldweb1.jlab.org/wiki/images/4/49/S10362-33\\_series\\_kapd1023e05.pdf](https://halldweb1.jlab.org/wiki/images/4/49/S10362-33_series_kapd1023e05.pdf).
- [8] <https://geant4.web.cern.ch/geant4/>.
- [9] K. S. Krane, Introductory Nuclear Physics, John Wiley & Sons, 1988, Ch. Detecting Nuclear Radiations, pp. 201–202.
- [10] C. M. Poole, A cad interface for geant4, paper submitted to Cornell Archive (arXiv) May 5, 2011 (2011). URL <http://arxiv.org/pdf/1105.0963.pdf>
- [11] A. L. . C. Moison, A more physical approach to model the surface treatment of scintillation counters and its implementation into detect, paper presented at IEEE, Nuclear Science Symposium; Anaheim, November 2-4 available at <http://geant4.slac.stanford.edu/UsersWorkshop/PDF/Peter/moisan.pdf> (1996).
- [12] P. Khetarpal, Start Counter Geant4 Simulations, start Counter Geant4 Simulations Wiki available at [https://halldweb.jlab.org/wiki/index.php/Start\\_Counter\\_Simulations](https://halldweb.jlab.org/wiki/index.php/Start_Counter_Simulations).
- [13] <https://www.newport.com/p/MT-XYZ>.
- [14] P. Khetarpal, Start counter: Optics simulations, talk Given at the February 16, 2012 GlueX Collaboration meeting (2012). URL [https://halldweb.jlab.org/DocDB/0019/001921/002/khetarpal\\_feb2012.pdf](https://halldweb.jlab.org/DocDB/0019/001921/002/khetarpal_feb2012.pdf)
- [15] <https://shop.buehler.com/consumables/grinding-polishing/polishing-suspensions/alumina-suspensions>.
- [16] <http://www.caswellplating.com/buffing-polishing/buffing-wheels/canton-flannel-wheels.html#>.
- [17] [https://www.novuspolish.com/polish\\_mates.html](https://www.novuspolish.com/polish_mates.html).
- [18]  $^{90}\text{Sr}$  Decay Radiation Data, national Nuclear Data Center, Nuclear Structure and Decay Database (NuDat) available at <http://www.nndc.bnl.gov/nudat2/decaysearchdirect.jsp?nuc=90SR&unc=nds>.
- [19]  $^{90}\text{Y}$  Decay Radiation Data, national Nuclear Data Center, Nuclear Structure and Decay Database (NuDat) available at <http://www.nndc.bnl.gov/nudat2/decaysearchdirect.jsp?nuc=90Y&unc=nds>.
- [20] <http://www.dupont.com/products-and-services/membranes-films/pvf-films.html>.
- [21] H. Dong, Description and Instructions for the Firmware of Processing FPGA of the ADC250 Boards Version 0x0C0D, fADC250 Manual Available at [https://coda.jlab.org/drupal/system/files/pdfs/HardwareManual/fADC250/FADC250\\_Processing\\_FPGA\\_Firmware\\_ver\\_0x0C0D\\_Description\\_Instructions.pdf](https://coda.jlab.org/drupal/system/files/pdfs/HardwareManual/fADC250/FADC250_Processing_FPGA_Firmware_ver_0x0C0D_Description_Instructions.pdf) (February 2017).
- [22] E. Smith, Low-level calibration constants for BCAL, technical note GlueX-doc-2618-v10, available at

- [https://halldweb.jlab.org/DocDB/0026/002618/011/bcal\\_constants.pdf](https://halldweb.jlab.org/DocDB/0026/002618/011/bcal_constants.pdf) (December 2014).
- [23] <https://root.cern.ch/doc/master/classTMinuit.html>.
- [24] J. B. et al. (Particle Data Group), Review of particle physics, Phys. Rev. D 86 (010001) (2012) 342–343.
- [25] B. Zihlmann, GlueX Time Of Flight Calibration, technical note GlueX-doc-2767-v4 available at <https://halldweb.jlab.org/DocDB/0027/002767/005/tofcalib.pdf> (July 2015).
- [26] P. Mattione, RF Calibration, rF Calibration Wiki available at [https://halldweb.jlab.org/wiki/index.php/RF\\_Calibration](https://halldweb.jlab.org/wiki/index.php/RF_Calibration).
- [27] P. Vavilov, Ionization losses of high-energy particles, Journal of Experimental and Theoretical Physics 5 (4) (1957) 749–751.
- [28] S. Seltzer, M. Berger, Studies in Penetration of Charged Particles in Matter, National Academy of Sciences - National Research Council, 1964, Ch. Energy-Loss Straggling of Protons and Mesons: Tabulation of the Vavilov Distribution, pp. 187–203.
- [29] B. Schorr, Programs for the landau and the vavilov distributions and the corresponding random numbers, Computer Physics Communications 7 (1974) 215–224.